Interaction of Electrons and Neutrinos with Nuclei

J.A. Caballero[1], **G.D. Megias**[1], **J. E. Amaro**[2], **M. B. Barbaro**[3], **T. W. Donnelly**[4], **I. Ruiz Simo**[2]

[1]Departamento de Física Atómica, Molecular y Nuclear, Universidad de Sevilla, 41080 Sevilla, Spain

[2]Departamento de Física Atómica, Molecular y Nuclear and Instituto Carlos I de Física Teorica y Computacional, Universidad de Granada, 18071 Granada, SPAIN

[3]Dipartimento di Fisica, Università di Torino and INFN, Sezione di Torino, Via P. Giuria 1, 10125 Torino, Italy

[4]Center for Theoretical Physics, Laboratory for Nuclear Science and Department of Physics, Massachusetts Institute of Technology, Cambridge, MA 02139, USA

Abstract. We present our modeling of electron-nucleus reactions and compare its predictions with inclusive ^{12}C (e, e') experimental data. The model is based on the supercaling phenomenon and the Relativistic Mean Field theory. We also discuss the impact of meson-exchange currents (MEC) and include the complete inelastic spectrum. The study is finally extended to the description of charged-current (CC) and neutral-current (NC) neutrino-nucleus reactions, and comparison with recent experiments spanning an energy range from hundreds of MeV up to 100 GeV is provided.

1 Introduction

One of the challenging goals of current neutrino oscillation experiments is a proper and precise description of neutrino-nucleus scattering at intermediate energies. In recent years, several models, originally developed to study electron-nucleus scattering, have been further extended to the description of neutrino-nucleus cross sections [1–8]. These models are required to provide a precise enough description of electron scattering data before they can be applied to neutrino reactions. Hence a consistent and complete description of the electron scattering cross section that includes not only the quasielastic (QE) regime, but also regions at higher energy transfer (nucleon resonances, inelastic spectrum), is essential for the analysis of current neutrino oscillation experiments.

Scaling [9] and superscaling properties [10–12] of electron-nucleus interactions have been analyzed in detail and used to construct a semi-phenomenological model for lepton-nucleus scattering [1]. This model, denoted as SuperScaling

Approach (SuSA), assumes the existence of universal scaling functions for electromagnetic and weak interactions. Recently we have developed an improved version of the superscaling model, called SuSAv2 [13], that incorporates relativistic mean field (RMF) effects [14–16] in the longitudinal and transverse nuclear responses, as well as in the isovector and isoscalar channels independently. Ingredients beyond the impulse approximation (IA), namely, 2p-2h MEC effects, have been shown to play an important role in the "dip" region between the QE and the Δ peaks. Here we extend the 2p-2h excitations to neutrino-nucleus reactions by evaluating the weak (with *vector* and *axial* components) charged meson-exchange currents, in both longitudinal and transverse channels.

The general study of CCQE neutrino/antineutrino scattering has been also extended to NC processes. Here the cross section depends on the strangeness content in the nucleon, particularly, through the axial form factor. The analysis of these processes may shed light on our present knowledge of the weak nucleon form factors, providing information that complements the one obtained from parity-violating (PV) electron scattering processes [17–19].

2 Inclusive Electron Scattering Processes

The double differential (e, e') inclusive cross section is given as the sum of two response functions corresponding to the longitudinal, R_L, and transverse, R_T, channels,

$$\frac{d^2\sigma}{d\Omega_e d\omega} = \sigma_{Mott}(v_L R_L + v_T R_T), \tag{1}$$

where σ_{Mott} is the Mott cross section and the vs are kinematical factors that involve leptonic variables (see [9] for explicit expressions). In terms of the scaling functions the nuclear responses are

$$R_{L,T}(q,\omega) = \frac{1}{k_F}\left[f_{L,T}^{T=1}(\psi')G_{L,T}^{T=1}(q,\omega) + f_{L,T}^{T=0}(\psi')G_{L,T}^{T=0}(q,\omega)\right], \tag{2}$$

where k_F is the Fermi momentum and the fs are the scaling functions, that only depend on the scaling variable ψ'. This scaling variable depends on q, ω and on the energy shift, E_{shift}, needed in order to have the corresponding scaling function peak located at $\Psi' = 0$. The functions $G_{L,T}^{T=0,1}$ are defined as the isoscalar and isovector responses of a moving nucleon and include relativistic corrections arising from the presence of the medium. Their explicit expressions can be found in [9, 13].

In spite of the merits of the RMF description, a particular drawback of the RMF concerns its dependence upon the momentum transfer q: indeed the RMF peak position keeps growing with q, thus making questionable the validity of the model at very high q. In fact, the large kinetic energy of the outgoing nucleon at very high q should make the final state interactions (FSI) effects negligible. Thus, it would be desirable that the RMF scaling functions approach the Relativistic Plane Wave Impulse Approximation (RPWIA) ones for increasing

momentum transfer [13]. This was a basic motivation in the development of a new SuperScaling Approach as a combination of RMF and RPWIA scaling functions where the first dominates at low to intermediate q and the latter at high q. This implies that the scaling functions in Eq. (2) should be replaced by linear combinations of RMF-based ($\tilde{f}_{L,T}$) and RPWIA ($\tilde{f}_{L,T}^{RPWIA}$) scaling functions:

$$
\begin{aligned}
\mathcal{F}_L^{T=0,1} &\equiv \cos^2 \chi(q) \tilde{f}_L^{T=0,1} + \sin^2 \chi(q) \tilde{f}_L^{RPWIA} \\
\mathcal{F}_T &\equiv \cos^2 \chi(q) \tilde{f}_T + \sin^2 \chi(q) \tilde{f}_T^{RPWIA} ,
\end{aligned}
\tag{3}
$$

where $\chi(q)$ is a q-dependent angle given by

$$
\chi(q) \equiv \frac{\pi}{2} \left(1 - \left[1 + e^{\left(\frac{(q-q_0)}{\omega_0} \right)} \right]^{-1} \right)
\tag{4}
$$

and the transition between RMF and RPWIA behaviors occurs at intermediate q-values (q_0) in a region of width ω_0, which is fixed at 200 MeV.

The extension of the model to the inelastic region implies the hadronic tensor to be given in the form [20]:

$$
W_{inel}^{\mu\nu}(\mathbf{q}, \omega) = \frac{3\mathcal{N}}{4\pi k_F^3} \int_F d\mathbf{h} \frac{m_N}{\bar{E}_h} w_{inel}^{\mu\nu}(H, Q, \omega + \bar{E}_h)
\tag{5}
$$

with H and $\overline{E}_h = \sqrt{h^2 + m_N^2}$ the 4-momentum and energy of the on-shell nucleon in the nucleus attached to the virtual photon.

2.1 Results

In this section we present our results for ^{12}C(e, e') cross sections. We adopt the Bosted and Christy parametrization for the single-nucleon inelastic structure functions [21,22] which describes DIS (Deep Inelastic Scattering), resonant and non-resonant regions. For the QE regime, we employ the electromagnetic form factors of the extended Gari-Krumpelmann (GKex) model [23–25]. Additionally, for the Fermi momentum we employ the values obtained in [12], namely $k_F = 228$ MeV/c for ^{12}C. Results are shown in Figure 1: in each panel we show the three separate contributions to the inclusive cross section, namely, QE, 2p-2h MEC and inelastic. The comparisons are carried out for a wide range of kinematics from low-intermediate energies to the highly-inelastic regime. Results illustrate that for electrons scattered backwards, the q-values corresponding to the inelastic process are smaller than those ascribed to the QE regime. However, notice that in this situation the cross section is clearly dominated by the QE peak. On the contrary, at very forward kinematics the inelastic process takes place at larger values of q. Thus, the two regimes, QE and inelastic, overlap strongly, the inelastic processes being the main ones responsible for the large cross sections observed at increasing values of ω. Finally, for intermediate scattering angles the behavior of q exhibits a region where it decreases (QE-dominated process),
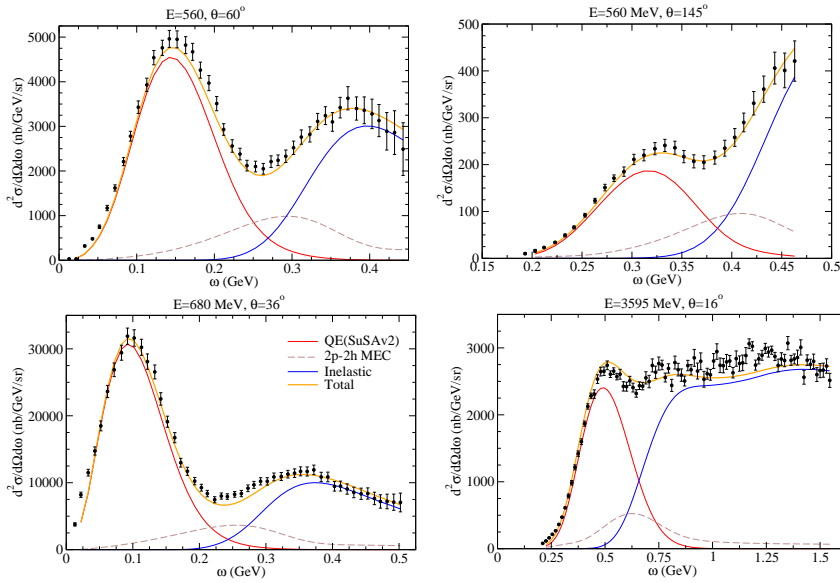
Figure 1. (Color online) Comparison of inclusive ^{12}C(e,e') cross sections and predictions of the QE-SuSAv2 model (red line), 2p-2h MEC model (dashed brown line) and inelastic-SuSAv2 model (blue line). The sum of the three contributions is represented with a solid orange line.

whereas for higher ω (inelastic regime) the behavior of q reverses and starts to go up. In these situations the QE peak, although significantly overlapped with the inelastic contributions, is clealy visible even for very high electron energies.

The analysis presented in Figure 1 demonstrates that the present SuSAv2-MEC model provides a very successful description of the whole set of (e, e') data, validating the reliability of our predictions. The positions, widths and heights of the QE peak are nicely reproduced by the model taking into account not only the QE domain but also the contributions given by the 2p-2h MEC terms (around $\sim 10 - 15\%$).

To conclude, the accordance between theory and data in the inelastic regime, where a wide variety of effects are taken into account, also gives us a great confidence in the reliability of our calculations. Note the excellent agreement in some situations even being aware of the limitations and particular difficulties in order to obtain phenomenological fits of the inelastic structure functions, and the poorer quality of some experimental data sets at these kinematics. A complete analysis covering a very wide range of kinematics is given in [26].

3 Charged-Current Neutrino-Nucleus Reactions

The double differential (ν_l, l') cross section is given as the sum of longitudinal (L) and transverse (T) channels, each of them composed of pure vector (VV) and axial components (AA), and the interference transverse (T') vector-axial channel (VA), which is constructive (+) for neutrino scattering and destructive (-) for antineutrino one:

$$\frac{d\sigma}{dk_\mu d\Omega} = \sigma_0 \left(\hat{V}_L R_L + \hat{V}_T R_T \pm 2\hat{V}_{T'} R_{T'} \right) , \qquad (6)$$

where

$$\hat{V}_L R_L = \hat{V}_{CC} R_{CC} + 2\, \hat{V}_{CL} R_{CL} + \hat{V}_{LL} R_{LL} , \qquad (7)$$

$\hat{V}_K$ are kinematical factors, R_K are the nuclear response functions and

$$\sigma_0 = \frac{\left(G_F^2 \cos\theta_c \right)^2}{2\pi^2} \left(k' \cos\frac{\tilde{\theta}}{2} \right)^2 \qquad (8)$$

depends on the Fermi constant G_F, the Cabibbo angle θ_c, the outgoing lepton momentum k', and the generalized scattering angle $\tilde{\theta}$.

In this work we evaluate the nuclear responses by employing the SuSAv2 model. Concerning the description of the 2p-2h MEC, we employ a calculation performed within the relativistic Fermi gas model in which a fully Lorentz covariant analysis can be achieved. Finally, we consider an extension of the SuSAv2 model to the region where the Δ-excitation dominates.

In Figure 2 we show the double differential cross section averaged over the neutrino (antineutrino) energy flux against the kinetic energy of the final muon. Left (right) panels correspond to neutrino (antineutrino) scattering on ^{12}C. Data are taken from the MiniBooNE collaboration [27]. We represent a few representative kinematical situations where each panel refers to results averaged over a particular muon angular bin (see [28] for a whole analysis). Notice that the mean energy of the MiniBooNE ν_μ ($\overline{\nu}_\mu$) flux is 788 (665) MeV. These high energies require a fully relativistic treatment of the process.

Note how the theoretical prediction including both the QE and the 2p2h-MEC effects gets in great accordance with data. This is particularly true for neutrinos (left panels). On the contrary, in the case of antineutrinos (right panels) the discrepancy between theory and data tends to increase as θ_μ gets larger. Notice, however, that in these situations data are not very representative. Results in Figure 2 clearly show the relevant role played by effects beyond the impulse approximation. As shown, the contribution of the 2p2h-MEC effects is very relevant for both neutrinos and antineutrinos being their relative percentage at the maximum, compared with the pure QE response, of the order of $\sim 25-35\%$. The relative strength associated to 2p2h-MEC gets larger for increasing values of the angle, particularly, in the case of antineutrinos.
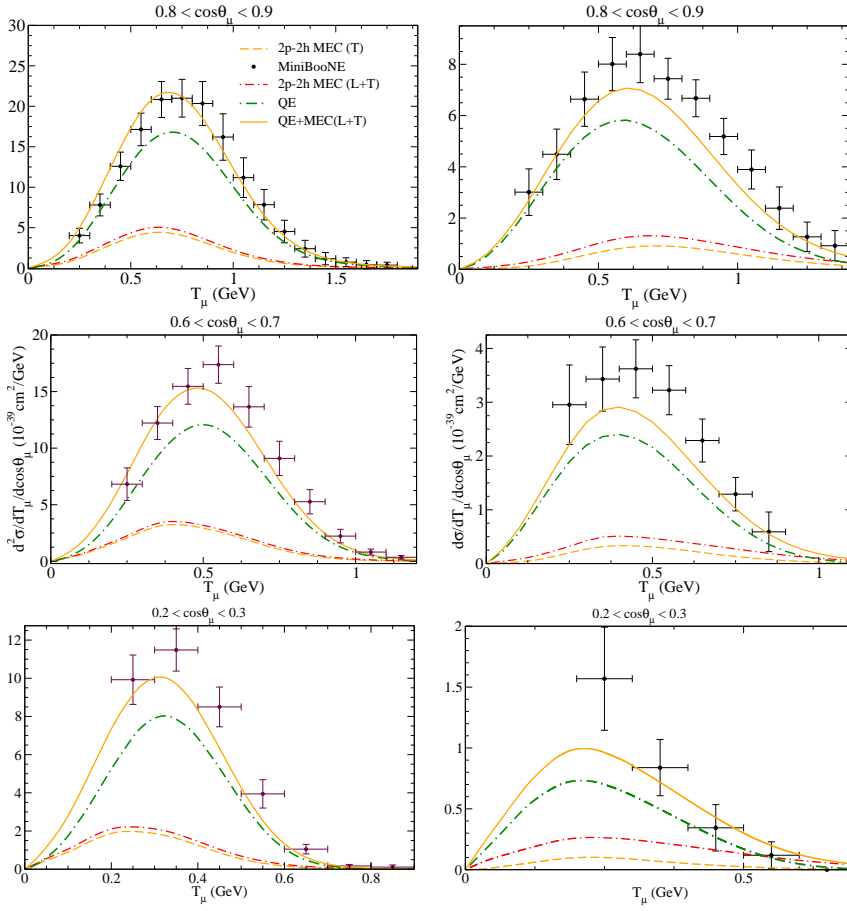
Figure 2. (Color online) MiniBoone neutrino (left panels) and antineutrino (right) double differential cross sections.

4   Neutral-Current Neutrino-Nucleus Processes

The general formalism for NC neutrino (antineutrino) scattering reactions in the quasielastic (QE) regime has been introduced in several previous works [29–33]. Here we simply summarize those aspects which are of more relevance for later discussion of results. In this section we restrict ourselves to the impulse aproximation. The relativistic one-body current operator modeling the coupling between the virtual Z boson and the bound nucleon depends on the weak vector form factors that can be related to the corresponding electromagnetic ones by the conserved vector current (CVC) hypothesis. Additional dependence on the electric, magnetic and axial strangeness should be considered as well.

In what follows we analyze the uncertainties linked to the several ingredients entering the description of the observables, particularly, the cross section and proton-neutron ratio. For a general review of the basic expressions of the neutral weak nucleon form factors and the specific set of parameters considered in the calculations see [17].

4.1 NCQE Cross Section

We start by analyzing the behavior of the neutral-current differential cross section as a function of the nucleon kinetic energy for several fixed values of the incident neutrino energy. In Figure 3 we present the NCQE neutrino-^{12}C cross section computed with different nuclear models: RMF, RPWIA and SuSA. We also include for reference the relativistic Fermi Gas (RFG) model. Each panel corresponds to a different value of ε_ν. These span the energy range in which the MiniBooNE flux (see [34, 35]) has a significant weight. The free proton cross section ($\times 2$) is also represented in order to estimate its contribution to the total CH_2 cross section.
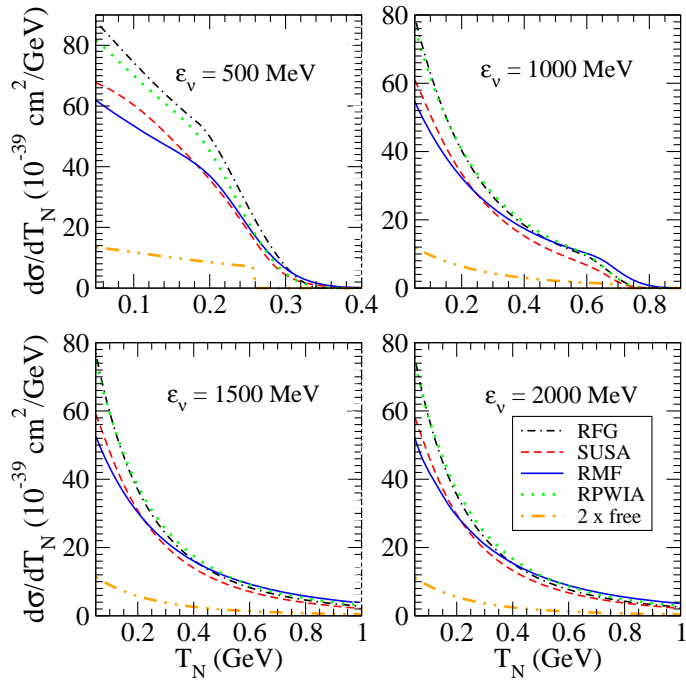

Figure 3. NCQE ^{12}C cross section computed using the RMF (solid blue), SUSA (dashed red), RFG (dot-dashed black) and RPWIA (dotted green) models. The free proton cross section ($\times 2$) is also represented (two-dot-dashed orange).

As observed, the main difference introduced by the nuclear model is linked to the treatment of final state interactions (FSI). Note that the two models that do not incorporate FSI, that is, RFG and RPWIA, give rise to very similar results, the discrepancy being only clearly visible for the lowest neutrino energy considered: $\varepsilon_\nu = 500$ MeV. For larger values the differences tend to disappear. With regards to SuSA and RMF, that account for FSI, the cross sections are significantly reduced with respect to the previous models being their discrepancy smaller.

The impact of the strange parameters on the cross section is shown in Figure 4 where we have selected the value $\varepsilon_\nu = 500$ MeV and the RMF approach. The discussion of results follows the same general trends for other kinematics and/or nuclear models. The role of the magnetic strangeness, μ_s, is presented in the top panel, while the electric strangeness, ρ_s, is considered in the bottom one. As shown, the cross section for ^{12}C-protons and -neutrons for two extreme values of μ_s leads to very similar results. In fact, the effect of μ_s on the total cross section is negligible due to the cancellation between the contributions associated to protons and neutrons. The same effect occurs for the electric
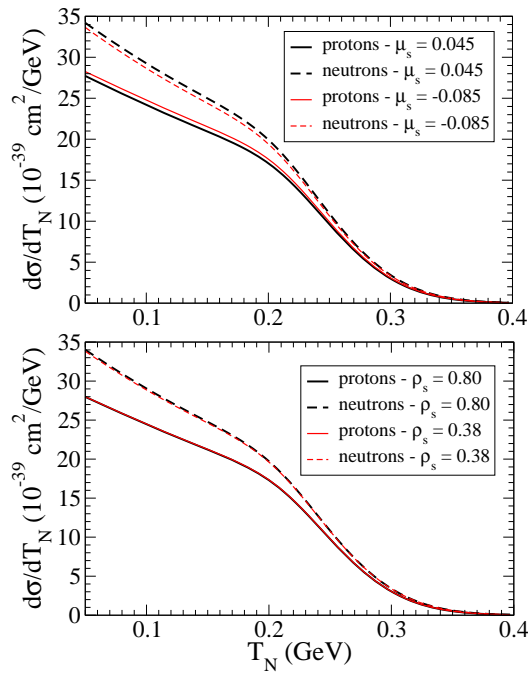

Figure 4. NCQE proton (solid lines) and neutron (dashed lines) cross sections computed using the RMF model. In top (bottom) panel the influence of the magnetic (electric) strange parameter is studied.
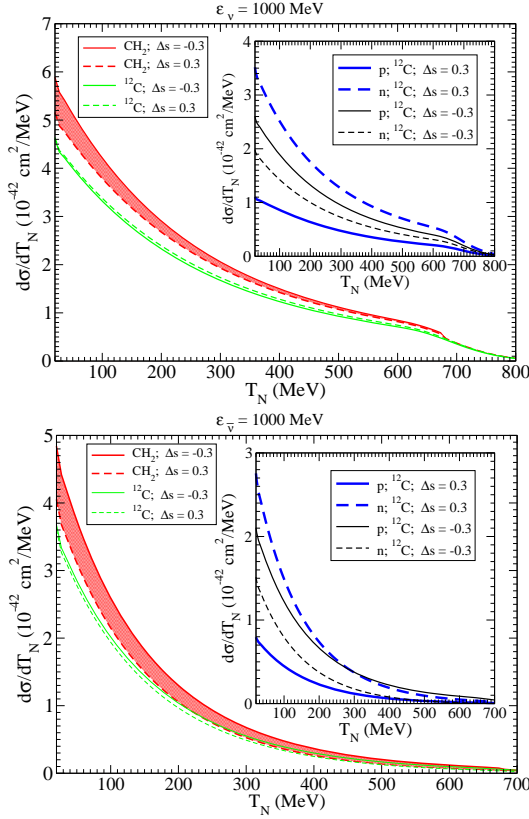
Figure 5. NCQE cross sections for neutrinos (top) and antineutrino (bottom) computed using the RMF model. Results for ^{12}C and CH_2 are presented. In inner panel the separate contribution in ^{12}C for protons and neutrons is displayed.

strange parameter (bottom panel in Figure 4), but in this case the role of electric strangeness is negligible on the separate proton and neutron cross sections. This result emerges because ρ_s is linked to the longitudinal response which is very strongly suppressed for neutrino/antineutrino cross sections.

The effects introduced by the axial strangeness, $g_A^{(s)}$, are analyzed in Figure 5. The RMF model has been considered and the neutrino (antineutrino) energy has been fixed to 1 GeV. As observed, the cross section for neutrino/antineutrino scattering on ^{12}C shows almost no dependence with the axial strangeness. This is due to the different role played by strangeness for protons and neutrons (see inner panels in the figures). In the case of protons the cross section gets enlarged for negative values of g_A^s, whereas the reverse occurs for neutrons. These opposite effects tend to cancel for isoscalar nuclei, hence leading to a negligible effect in the total cross section.
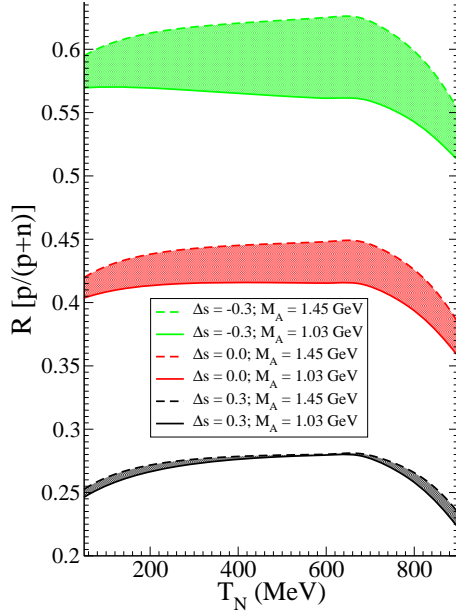
Figure 6. Ratio computed within the RMF. Results correspond to two different values of the axial mass: the world-average $M_A = 1.03$ GeV/c and $M_A = 1.45$ GeV/c. Moreover, three different values for the axial strangeness have been considered: $\Delta s = -0.3$ (green region), $\Delta s = 0$ (red) and $\Delta s = 0.3$ (dark-blue).

It is also important to discuss the effects introduced by considering mineral oil, CH_2, as a target. This is the situation for the MiniBooNE experiment. As shown, the role of the two protons leads to a significant enhancement (larger for negative axial strangeness) of the total cross section. The use of CH_2 breaks the symmetry of the cross section with the axial strangeness. This is represented by the shadowed areas in Figure 6 that represent the uncertainty linked to the axial strangeness.

4.2 Proton-neutron ratio

To conclude we study the dependence of the proton-neutron ratio with the axial strangeness and axial mass. We define the ratio as

$$R \equiv \frac{\sigma_p}{\sigma_p + \sigma_n} \, , \tag{9}$$

where σ_p (σ_n) is the cross section of ^{12}C-protons (-neutrons).

Results are shown in Figure 6 where we have selected the neutrino energy $\varepsilon_\nu = 1000$ MeV and the RMF. In what follows we do not consider the role played by the electric and magnetic strangeness as these effects in the ratio

57

are negligible compared with the uncertainty linked to the axial mass, M_A, and/or g_A^s. In Figure 6 each colored band represents a specific value of the axial strangeness, i.e, $g_A^s = 0.3$ (grey), $g_A^s = 0$ (red) and $g_A^s = -0.3$ (green). The clear separation between the three bands reflects the high sensitivity of the proton/neutron ratio with the axial strangeness. On the contrary, the effects introduced by the axial mass are significantly smaller. This is illustrated in each band by the shadowed region. The lower limit corresponds to the world-average value $M_A = 1.03$ GeV/c while the upper one shows the result corresponding to $M_A = 1.45$ GeV/c. It is also important to point out how the relative effect introduced by the axial mass depends on the particular value of the strangeness. This shows a correlation between both parameters. The ratio is very insensitive to M_A for $g_A^s = 0.3$ (grey band), whereas for negative $g_A^s = -0.3$ the uncertainty is of the order of $\sim 10 - 12\%$. On the contrary, the change in the axial strangeness leads to variations in the ratio that differ by a factor ~ 1.5 (for correlative values in g_A^s). This analysis shows the importance of the proton/neutron ratio as an observable excellently suited to get precise information on the axial strangeness content in the nucleon.

Acknowledgements

References

[1] J.E. Amaro, M.B. Barbaro, J.A. Caballero, T.W. Donnelly, A. Molinari and I. Sick, *Phys. Rev. C* **71** (2005) 015501.

[2] J.E. Amaro, M.B. Barbaro, J.A. Caballero, T.W. Donnelly, J.M. Udias, *Phys. Rev. C* **75** (2007) 034613.

[3] M. Martini, M. Ericson, G. Chanfray and J. Marteau, *Phys. Rev. C* **80** (2009) 065501.

[4] A. Meucci, C. Capuzzi, C. Giusti, and F.D. Pacati, *Phys. Rev. C* **67** (2003) 054601.

[5] A. Meucci, C. Giusti, and F.D. Pacati, *Nucl. Phys. A* **739** (2004) 277.

[6] J. Nieves, J.E. Amaro, and M. Valverde, *Phys. Rev. C* **70** (2004) 055503.

[7] O. Benhar, P. Coletti and D. Meloni, *Phys. Rev. Lett.* **105** (2010) 132301.

[8] O. Lalakulich, K. Gallmeister, and U. Mosel, *Phys. Rev. C* **86** (2012) 014614.

[9] D.B. Day, J.S. McCarthy, T.W. Donnelly, and I. Sick, *Annu. Rev. Nucl. Part. Sci.* **40** (1990) 357.

[10] T.W. Donnelly and I. Sick, *Phys. Rev. Lett.* **82** (1999) 3212.

[11] T.W. Donnelly and I. Sick, *Phys. Rev. C* **60** (1999) 065502.

[12] C. Maieron, T.W. Donnelly and I. Sick, *Phys. Rev. C* **65** (2002) 025502.

[13] R. Gonzalez-Jimenez, G.D. Megias, M.B. Barbaro, J.A. Caballero, and T.W. Donnelly, *Phys. Rev. C* **90** (2014) 035501.

[14] J.A. Caballero, J.E. Amaro, M.B. Barbaro, T.W. Donnelly, C. Maieron and J.M. Udias, *Phys. Rev. Lett.* **95** (2005) 252502.

[15] J. A. Caballero, *Phys. Rev. C* **74** (2006) 015502.

[16] J. A. Caballero, J.E. Amaro, M.B. Barbaro, T.W. Donnelly, and J.M. Udias, *Phys. Lett. B* **653** (2007) 366.

[17] R. Gonzalez-Jimenez, J. A. Caballero and T. W. Donnelly, Phys. Rep. **524**, 1 (2013).

[18] M. J. Musolf and T. W. Donnelly, *Nucl. Phys. A* **546** (1992) 509.

[19] M. J. Musolf *et al.*, *Phys. Rep.* **239** (1994) 1.

[20] M. B. Barbaro, J. A. Caballero, T. W. Donnelly and C. Maieron, *Phys. Rev. C* **69** (2004) 035502.

[21] P. E. Bosted and M. E. Christy, *Phys. Rev. C* **77** (2008) 065206.

[22] P. E. Bosted and M. E. Christy, *Phys. Rev. C* **81** (2010) 055213.

[23] E.L. Lomon, *Phys. Rev. C* **64** (2001) 035204.

[24] E.L. Lomon, *Phys. Rev. C* **66** (2002) 045501.

[25] C. Crawford *et al.*, *Phys. Rev. C* **82** (2010) 045211.

[26] G.D. Megias, J.E. Amaro, M.B. Barbaro, J.A. Caballero, and T.W. Donnelly, *Phys. Rev. D* **94** (2016) 013012.

[27] A.A. Aguilar-Arevalo *et al.* [MiniBooNE Collaboration], *Phys. Rev. D* **79** (2009) 072002.

[28] G.D. Megias, J.E. Amaro, M.B. Barbaro, J.A. Caballero, T.W. Donnelly, and I. Ruiz Simo, arXiv:1607.08565 [nucl-th] (2016).

[29] W.M. Alberico *et al.*, *Nucl. Phys. A* **623** (1997) 471.

[30] J.E. Amaro, M.B. Barbaro, J.A. Caballero and T.W. Donnelly, *Phys. Rev. C* **73** (2006) 035503.

[31] M.C. Martinez, P. Lava, N. Jachowicz, J. Ryckebusch, K. Vantournhout and J.M. Udias, *Phys. Rev. C* **73** (2006) 024607; [nucl-th/0505008].

[32] M.C. Martinez, J.A. Caballero, T.W. Donnelly and J.M. Udias, *Phys. Rev. C* **77** (2008) 064604; [arXiv:0805.2344 [nucl-th]].

[33] M.C. Martinez, J.A. Caballero, T.W. Donnelly and J.M. Udias, *Phys. Rev. Lett.* **100** (2008) 052502; [arXiv:0802.1745 [nucl-th]].

[34] A.A. Aguilar-Arevalo *et al.* [MiniBooNE Collaboration], *Phys. Rev. D* **82** (2010) 092005.

[35] A.A. Aguilar-Arevalo *et al.* [MiniBooNE Collaboration], arXiv:1301.7067 [hep-ex].